Rheologica Acta
https://doi.org/10.1007/s00397-022-01377-6

ORIGINAL CONTRIBUTION

Rheological investigation and modeling of healing properties during extrusion-based 3D printing of poly(lactic-acid)

Xavier Lacambra-Andreu[1,2] · **Xavier P. Morelle**[1] · **Abderrahim Maazouz**[1,3] · **Jean-Marc Chenal**[2] · **Khalid Lamnawar**[1]

Received: 28 September 2022 / Accepted: 1 November 2022

Abstract

The focus of the present paper is the rheological study of poly(D,L-lactic-acid) (PDLLA) towards a modeling of their healing properties during 3D direct pellet printing extrusion (DPPE). The viscoelastic properties of PDLLA and the filament temperature during deposition are first characterized. The influence of DPPE processing conditions is investigated in terms of temperature, time, and printing speed. For this, we propose a modeling of the process-induced interphase thickness between two deposited layers considering the non-isothermal polymer relaxation and accounting for the contribution of entanglement rate through the Convective constraint release model. Hence, taking into account the induced chain orientation and mobility coming from filament deposition, this model quantifies the degree of healing between 3D-printed layers. Eventually, the proposed model is validated by comparing the theoretically calculated degree of healing with experimental tensile properties and lap shear results.

Keywords 3D printing · Direct pellet printing extrusion · Rheology · Interface healing · Polymer diffusion · Modeling

Introduction

Direct Pellet Printing Extrusion (DPPE) is a recent additive manufacturing technique that produces modular parts directly from raw polymers in granulate form. In contrast to fused filament fabrication, DPPE is another FDM (Fused deposition modeling) technique that makes it possible to reduce thermal degradation by suppressing the filament preparation step. Thus, DPPE is particularly useful for additive manufacturing of thermally unstable polymers (Zhou et al. 2018). Despite some industrial research exploring the possibilities of DPPE, very few authors have studied the rheology of such process (Zhou et al. 2018; Gradwohl et al. 2021).

In recent years, more and more authors have shown interest in using additive manufacturing techniques for tissue engineering and regenerative applications thanks to their potential to elaborate personalized devices, and to reduce costs and production times (Do Vale Pereira et al. 2014; Corcione et al. 2017; Gradwohl et al. 2021). However, several aspects of the process, such as diminished mechanical properties compared to traditional processing methods, still impede the adoption of additive manufacturing for medical device applications. In particular, these limiting features involve strong anisotropic response and poor z-axis properties, which primarily come from poor interlayer adhesion.

During the 3D printing extrusion process, the melt experiences high shear rates in the nozzle, deformation during deposition, and large temperature changes during the welding process. All of these lead to strong non-equilibrium relaxations that will affect the polymer welding (Das et al. 2021). A number of recent studies have investigated the rheological behavior of the melt during the Fused Deposition Modeling (FDM) process (e.g., Seppala et al. 2017; McIlroy and Olmsted 2017b, a; Cicala et al. 2018; Peñas et al. 2020; Gilmer et al. 2021; Lepoivre et al. 2020; Das et al. 2021)). Furthermore, several articles modeled the

✉ Jean-Marc Chenal
jean-marc.chenal@insa-lyon.fr

✉ Khalid Lamnawar
khalid.lamnawar@insa-lyon.fr

[1] Université de Lyon, CNRS, UMR 5223, Ingénierie des Matériaux Polymères, INSA Lyon, Univ. Claude Bernard Lyon 1, Univ. Jean Monnet, F-69621 Villeurbanne, France

[2] Univ Lyon, INSA Lyon, Université Claude Bernard Lyon 1, CNRS, MATEIS, UMR5510, 69621 Villeurbanne, France

[3] Hassan II Academy of Science and Technology, 10100 Rabat, Morocco

heat transfer in an FDM process (Costa et al. 2015, 2017; Vanaei et al. 2021). Despite the recent papers dedicated to these subjects, relatively little research can be found when it comes to accounting for both rheology and heat transfer that occurs simultaneously during filament welding in 3D printing extrusion in non-isothermal conditions (Gilmer et al. 2021).

To gain a deeper comprehension of the 3D extrusion process, Costanzo et al. (2020) applied the Convective constraint release model (CCR) to account for the effect of the residual alignment of polymer chains at the filament-filament interfaces. They suggested that the lowered weld strength was mainly due to the flow-orientation through the nozzle and the deformation during the deposition process rather than due to a poor diffusion. In parallel, Gilmer et al. (2021) implemented a modeling approach to calculate the heat transfer, the degree of healing (D_h) and the residual stress induced during a non-isothermal welding.

In the present study, we explore through Small Amplitude Oscillatory Shear (SAOS) and capillary rheometry measurements the rheological properties of Poly(D,L-lactic acid) (PDLLA) used for DPPE. Through the use of a molecular mechanism framework (from reptation theory to CCR), the main objective of this manuscript is to present a thorough dialog between experimental and modeling results to predict the healing properties (and quantify the obtained interphases) of a printed filament. After that, the theory of crack healing (Wool and O'Connor 1981) is used to experimentally validate the modeling of the healing degree based on the interdiffusion thickness. For that purpose, experimental measurements of tensile properties and lap-shear tests on printed parts were performed and confronted to the obtained predictions.

Experimental section

Materials and preparation of model systems

Materials

An amorphous poly (D-lactide acid) hereafter referred to as PDLLA, with L-lactide content of around 82 wt%, a density of 1.24 g.cm^{-3},and a glass transition temperature (T_g) of 56 °C was supplied by Nature Works LLC (USA) (reference: PLA 4060D). Note that before the 3D extrusion step, PDLLA was dried for 4 h at 45 °C under a vacuum in order to prevent hydrolytic degradation during processing.

Printing process: direct pellet printing extrusion

A PAM Series Lx printer (Pollen AM, France) with four screw-based extruders was used for the manufacturing of the tensile and lap shear specimens. The Direct Pellet Printer was fed directly with polymer granulates, and the material was heated progressively thanks to the thermal control of the feeding zone, main extruder, and nozzle (Fig. 1).

All specimens were printed using a nozzle size of 0.4 mm and at a − 45°/45° orientation with a layer height of $H = 0.2$ mm, a filament width of $W = 0.4$ mm and a printing speed of $U_N = 30\mathrm{mm/s}$. The plateau temperature was set at 55 °C. The extruder temperature was set at 180 °C while the nozzle temperature was set at 190 °C. Five replicas were 3D-printed. Each specimen has a thickness of 6 layers (1.2 mm), and at the start of the printing, a skirt was printed around the specimen to verify and normalize the flow of the material before specimen elaboration.

Injection and compression molding

Conventional "bulk" specimens used as a reference for tensile testing were prepared on a HAAKE Minijet injection molding machine (Thermo Fisher Scientific, Cleveland, OH, USA). The injection molding procedure involved a cylinder temperature of 180 °C and a mold temperature of 55 °C under 800 bar of pressure for 20 s.

Specimens for lap-shear tests (see details in the "Experimental section" section) were obtained by compression

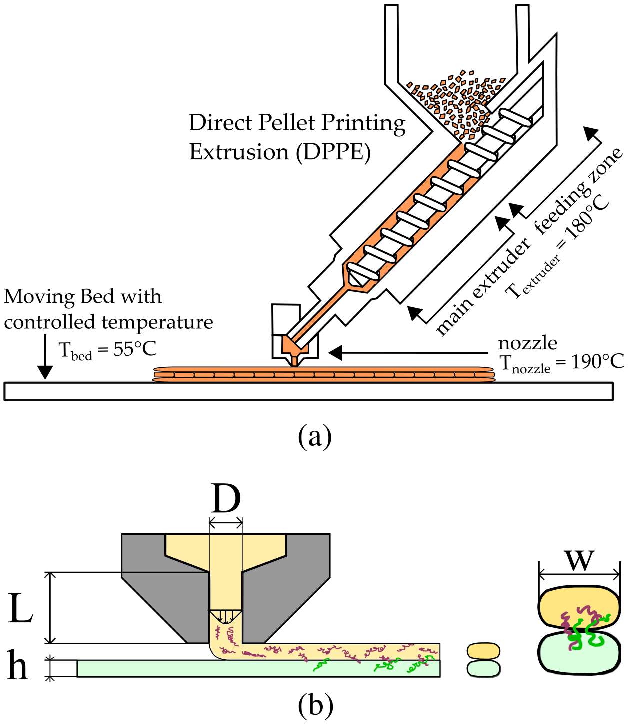

(a)

(b)

Fig. 1 **a** Schematic representation of the DPPE process. **b** Schematic representation of the deposition process and welding of filaments, highlighting chains interdiffusion with deposition time. D and L are respectively 0.4 mm and 2 mm molding. PDLLA granulates were pressed in a closed mold (145 × 145 × 1.5 mm) with a pressure of 10 MPa for 5 min at 140 °C. The prepared sheets were cut into squares with a side length of 25 mm. Finally, two PDLLA squares with a superposition length of 5 mm were placed into a mold at a temperature above T_g (56 °C) to create the lap-shear samples. A rectangular Kapton film was placed on top and bottom of the superposition area to facilitate the crack initiation. In order to favor a cohesive fracture, the ratio between the surface adhesion and the specimen thickness was adjusted. The level of adhesion between PDLLA sheets was regulated by modifying the healing time and temperature. The detailed assembly for lap-shear test are shown in Fig. 2.

Methods

Temperature monitoring and in-situ measurements

A K-type thermocouple ($d = 200$ µm), capable of measuring temperatures between 75 and 250 °C, was used to determine the temperature of filaments and interfaces between layers. The temperature was recorded with a time step resolution

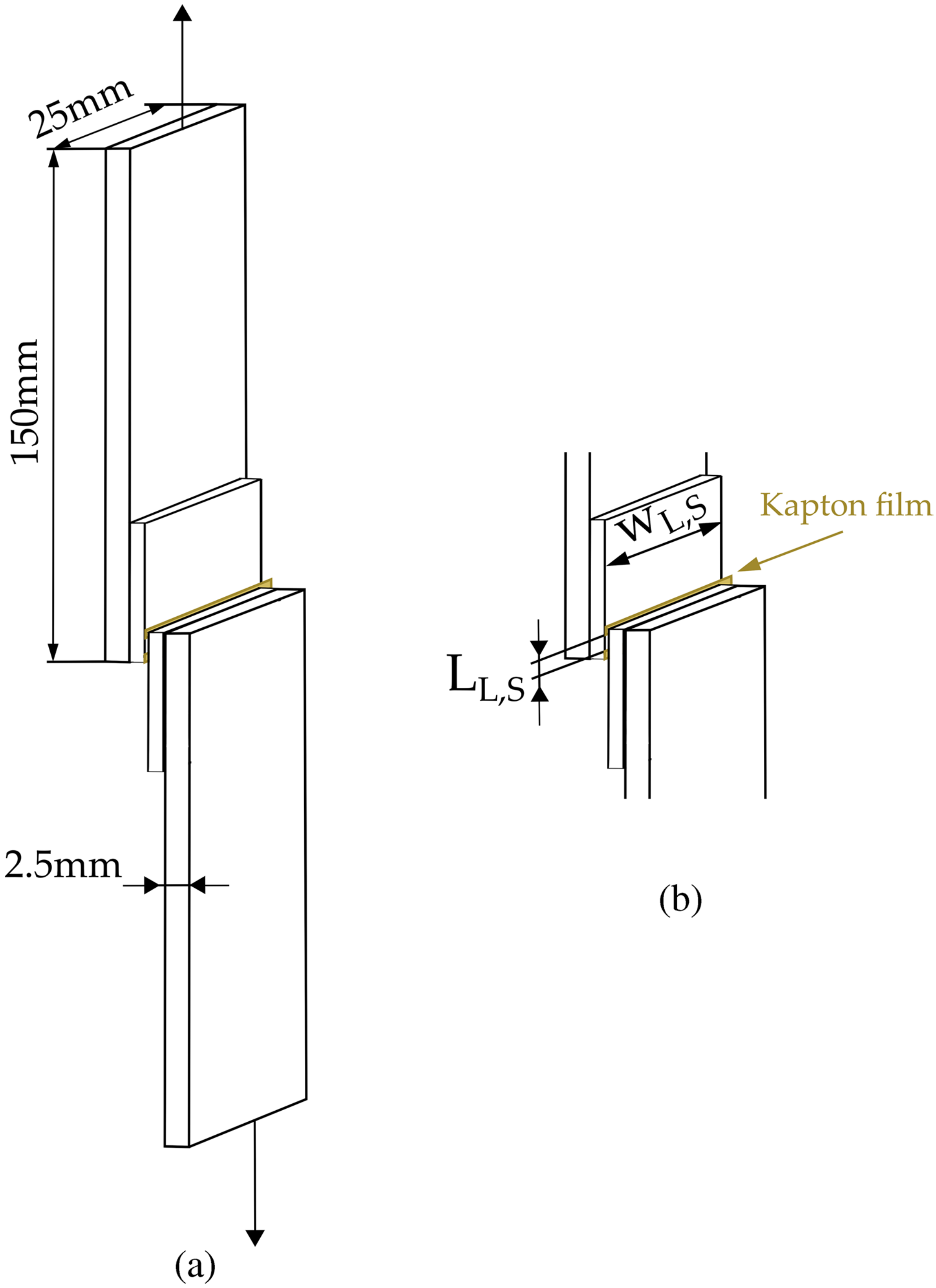

Fig. 2 **a** Lap shear assembly used in this work. **b** Lap shear sample diagram with the mask

of 0.2 s. The thermocouple was placed at the center of a dedicated (sacrificial) printed sample without disturbing the deposition process in order to get real *in-situ* data.

Rheological study

Small amplitude oscillatory shear rheology (SAOS) The SAOS melt rheological experiments were performed with a DHR-2 (TA Instruments, USA) stress-controlled rheometer using a parallel-plate geometry ($\varnothing = 25$ mm). Discs were prepared by hot pressing at 140 °C for 5 min at 200 bars. The disc specimens were placed between the plates, in a melted and relaxed state, and investigations were carried out at various temperatures under a continuous nitrogen purge. Dynamic frequency and time sweeps were performed in the linear viscoelastic regime at angular frequencies ranging from 0.1 to 628 $\text{rad} \cdot \text{s}^{-1}$ every 10 °C from 140 to 210 °C. After validating the thermorheological simplicity of PDLLA, time–temperature superposition was used to shift frequency data into a single master curve. The horizontal shift factor (a_t) was fitted to the Arrhenius and WLF equations.

Capillary rheometry Capillary flow measurements at a constant shear rate were carried out on a Malvern Rosand RH2000 (Bohlin Instruments, UK) capillary rheometer equipped with two barrels of 1 mm diameter. PDLLA was extruded through a capillary die with an entrance angle of 180°, length L, and diameter D. The apparent shear rates varied from 10 to 4000 s^{-1} and the temperature was set at 190 °C. The ratio L/D was varied from 10, 16, and 20 to account for the Bagley correction.

Dynamic mechanical analysis (DMA) DMA was conducted on parallelepipedic specimens ($h = 0.6$ mm, $w = 4.5$ mm and $L = 12$ mm). Frequency sweep tests were carried out using a DMA Q800 (TA Instruments, USA) in tensile mode. Viscoelastic master curves were obtained from frequency sweeps from 0.1 to 10 Hz at 0.05% strain every 10 °C from 60 to 110 °C. Time–temperature superposition was used to shift the frequency data into a single master curve. The horizontal shift factor (a_t) was fitted to the Williams-Landel-Ferry (WLF) equation.

Mechanical analysis

Lap-hear and Tensile tests were conducted using a universal AGSX 5 kN testing machine (Shimadzu Corporation, Ltd., Kyoto, Japan) with a crosshead speed of 1 mm/min. The reported results were averaged over five test specimens.

Uniaxial tensile tests Tensile testing was performed on dumbbell-shaped samples ($l_0 = 20$ mm, $w = 4.2$ mm, and $h = 1.2$ mm) for FDM and ($l_0 = 20$ mm, $w = 4.2$ mm, and $h = 2$ mm) for injection molding.

Shear strength under controlled conditions Lap-shear experiments were performed to characterize the interfacial cohesion. The bonded PDLLA–PDLLA joints ($w_{\mathrm{L,S}}$ = 25mm and $L_{\mathrm{L,S}}$ between 1.5 and 5 mm) were fractured in the lap shear geometry as shown in Fig. 2. The shear strength (σ_{h}) was calculated as the fracture load divided by the bonded area.

Results and discussion

Required input parameters for healing modeling

Heat transfer in transient conditions for DPPE

This part of our work reports the experimental measurements of layer temperature during deposition. In-situ temperature measurements have to be precise enough to record the temperature evolution of interfaces (e.g., the reheating peaks coming from the contact between new and previously deposited layers). Heat transfer during deposition is complex, with contributions from radiation, convection, and conduction. However, it has been demonstrated (a) that there is a loss of heat by convection with the environment, and (b) that the thermal contacts with the support and with adjacent filaments are the main contributors to the filament temperature evolution (Costa et al. 2015; Vanaei et al. 2021). The evolution of the temperature at the interfaces (measured at the center of the sample with a thermocouple type K) during the printing process of a tensile specimen is shown in Fig. 3a. The cooling of this first layer was significantly affected by the successive deposition of the following layers, which involved multiple reheating steps. However, the healing process mainly occurs after extrusion and during the deposition of the next layer. The temperature evolution during the very first seconds after deposition is faster than the acquisition time of the thermocouple. Thus, in order to obtain a thermal evolution of the interface for the first seconds after deposition, the cooling after the filament deposition was modeled by accounting for the extrusion temperature and the stabilized temperature is shown in Fig. 3b. Hereafter we present the heat transfer equation used to calculate the variation of the temperature as a function of time and position T (z, t) during the 3D printing process.

After filament deposition, we considered a transient homogeneous heat conduction in the filament from an initial temperature $T_i = T_{\mathrm{nozzle}}$ and with one boundary ($T_\infty = T_{\mathrm{plateau}}$). The thermal variation of the interface can be expressed as:

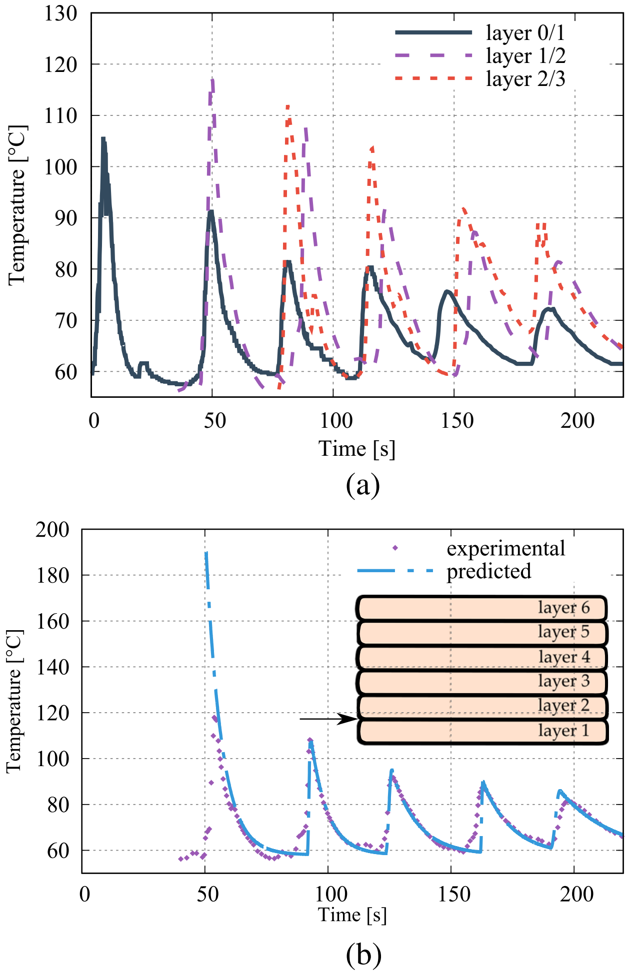

Fig. 3 **a** Temperature evolution of different interfaces and **b** experimental and modeled temperature evolution of the interface between layer 1 and 2 during printing at $T_{ext} = 190$ °C and $V_{imp} = 30$ mm/s for a tensile sample as a function of printing time

$$\frac{\partial T}{\partial t} = b\left(T_\infty - T\right) \tag{1}$$

with b the time constant (the fitting parameter extracted from Fig. 3):

$$b = \frac{h_{conv}\ A_s}{\rho V C_p} \tag{2}$$

With $h_{conv} = 150 W \cdot m^{-2} \cdot K^{-1}$ the convective heat transfer coefficient (Costa et al. 2015), A_s the specific area of the filament, ρ the density of PDLLA, V the volume of the filament and C_p the specific heat of PDLLA.integrating from $t = 0$, where $T = T_i$, to t, Eq. 1 gives:

$$T(t) = \left(T_i - T_\infty\right) \exp\left(-bt\right) + T_\infty \tag{3}$$

After each deposition, the temperature layer reached a constant value. The time between depositions observed in Fig. 3 depends on the geometry of the print and the deposition rate. Then, each following layer was deposited at the nozzle temperature with perfect contact with the previous deposited lower layer. The temperature of the lower layer increased due to the heating caused by the new layer deposition. Hence, the temperature evolution in the cross-section was predicted from the equation of unsteady state of heat conduction (Eq. 4). The thermal diffusivity between adjacent layers was adjusted to fit the experimental and theoretical reheating peaks.

$$\frac{\partial T}{\partial t} = \alpha \frac{\partial T^2}{\partial z^2} \tag{4}$$

with $\alpha = k/\rho C_p$ the thermal diffusivity and z the distance from the start of deposition (H the layer thickness).

Finally, Fig. 3b shows the modeled temperature profile of the interface between layers 1 and 2 during the 3D printing of a dumbbell-shaped bar.

Melt rheological study of the neat PDLLA

Prior to the elaboration process, SAOS and capillary measurements of PDLLA were performed to thoroughly determine the available processing window. The corrections of Rabinowitsch and Bagley were applied to calculate the real viscosity and corrected shear rates. Figure 4 presents an overview of the viscosity dependence on shear-rate. Cox-Merz rule was also applied. The complex viscosity of PDLLA presented the classic viscoelastic behavior, a plateau at low frequencies, and a shear-thinning behavior at high frequencies.

Then, the data was fitted with the Carreau-Yasuda theory (Eq. 5) to predict the viscosity as a function of the shear rate and other material coefficients (η_0, η_∞,τ, n):

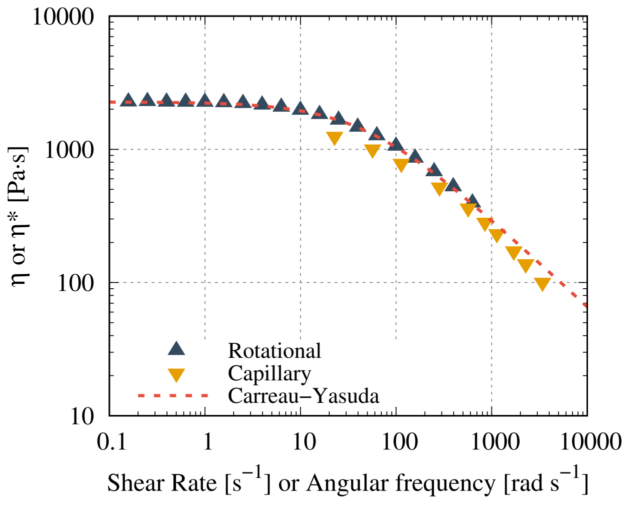

Fig. 4 Complex viscosity modulus (rotational) and corrected shear viscosity (capillary) respectively as a function of angular frequency and real shear rate for PDLLA at 190 °C

$$\eta = \eta_\infty + \left(\eta_0 - \eta_\infty\right)\left(1 + (\tau\dot{\gamma})^2\right)^{\frac{n-1}{2}} \tag{5}$$

here, $\dot{\gamma}$ is the shear rate, n the power law index ($n = 0.33$), $\eta_\infty = 0.1\mathrm{Pas}$, $\eta_0 = 2260\mathrm{Pas}$, and $\tau = 0.0294\mathrm{s}$.

In DPPE process, the viscosity of the polymer could be extrapolated from the presented curve (Fig. 4). From the flow rate applied with a printing speed of $U_\mathrm{n} = 30\mathrm{mms}^{-1}$ and knowing the die parameters, we could calculate a $\dot{\gamma} = 600\mathrm{s}^{-1}$ and estimated the real viscosity during the process ($\eta = 480\mathrm{Pas}^{-1}$). Hence, based on the previous result, it could be possible to tune and modify the printing parameters (i.e., temperature, speed, and nozzle diameter).

The time–temperature superposition master curve (G′, G″ at 190 °C) was calculated using the RepTate software to obtain the shift factors (Boudara et al. 2020). Figure 5a shows the master curve of the storage modulus G’ and loss modulus G’’ as functions of angular frequency at $T_\mathrm{ref} = 190°C$ for PDLLA by combining the results obtained by DMA and SAOS.

Four characteristic times were then evaluated. The number-average relaxation time, τ_n, corresponds to the inverse of the angular frequency at the intersection of G’ and G’’ ($\tau_\mathrm{n} = \eta_0 G_N^0$) and the weight-average relaxation time ($\tau_\mathrm{w} = \eta_0 J_0^e$), is the time corresponding to the maximum value of the Cole–Cole plot (Zhang et al. 2012;

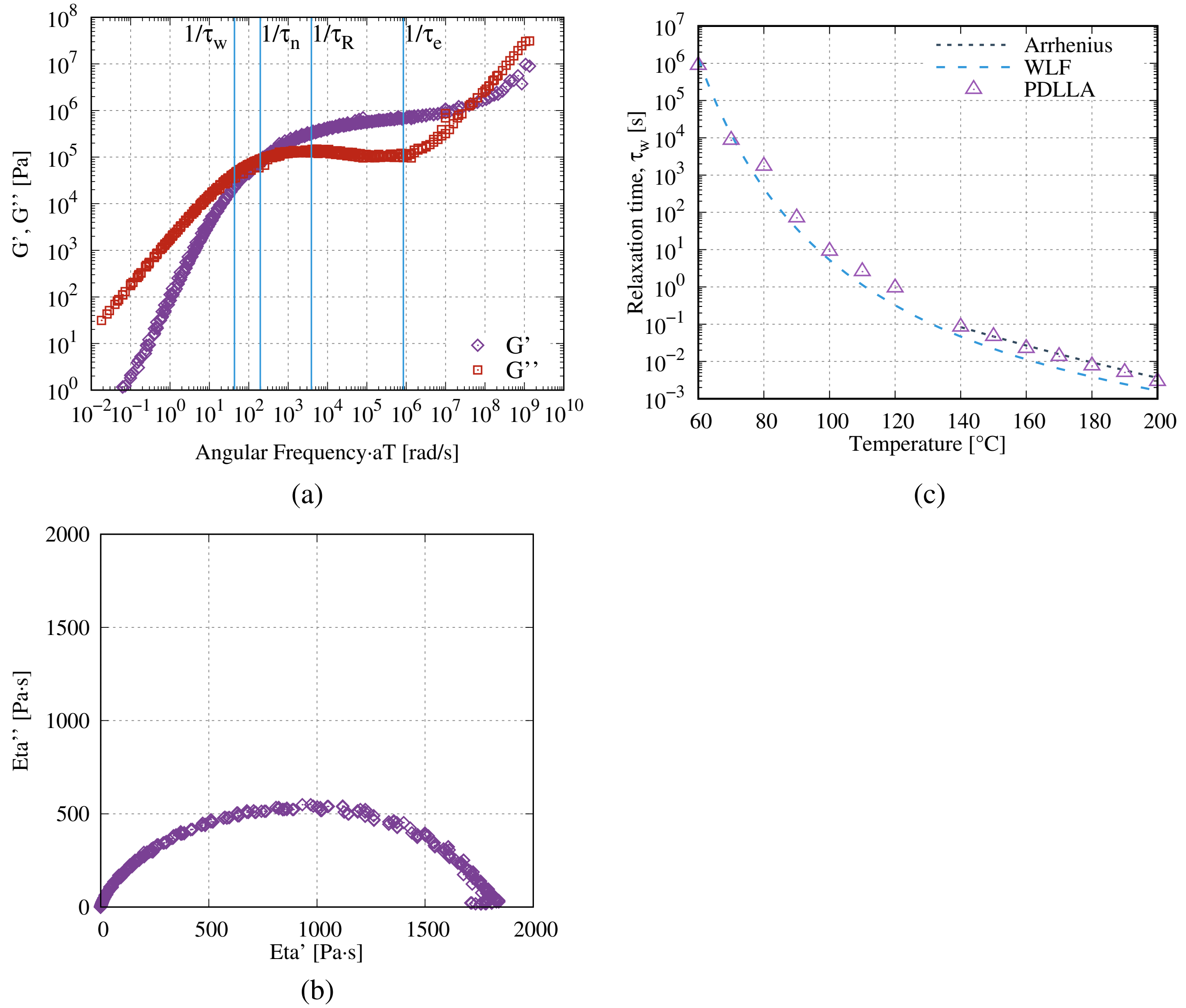

Fig. 5 Time–temperature superposition master curve of PDLLA at 190 °C from multiple frequency temperature sweeps for (**a**) G’, G’’ (**b**) Cole–Cole plots of imaginary viscosity (η^{ε}) versus real viscosity ($\eta^{'}$) and (**c**) temperature dependence of the relaxation times (τ_n) obtained from experimental results and fitted with the WLF and Arrhenius models. With, $E_\mathrm{a} = 84.13\mathrm{KJmol}^{-1}$ in the Arrhenius domain,$R = 8.314\mathrm{Jmol}^{-1}K^{-1}$,$C_1 = 6.03$, $C_2 = 156.54\mathrm{K}$ and $T_\mathrm{ref} = 190°\mathrm{C}$

Pei et al. 2017) (Fig. 5b). G_N^0 and J_0^e are respectively the rubbery plateau modulus and shear compliance modulus.

Figure 5c shows the evolution of τ_n as a function of temperature and the predicted behavior by the WLF and Arrhenius models. The relaxation time between entanglements, τ_e, and the Rouse time, τ_R, were determined experimentally from τ_w (here we assume τ_w as τ_{rep}):

$$\tau_w = 6\tau_R Z_e \tag{6}$$

$$\tau_R = \tau_e (Z_e)^2 \tag{7}$$

with Z_e, the number of entanglements at equilibrium (Z_e):

$$Z_e = \frac{\overline{M}_w}{M_e} \tag{8}$$

With $\overline{M}_w$ the weight average molecular mass and $M_e = 9200 g/mol$ the molecular weight between entanglements.

On the other hand, we have checked the average molecular weights of pellets and final specimens by SEC. Table 1 resumes the rheological properties as well as the molecular weights of neat PDLLA and 3D printed parts. The decrease in M_w indicates a degradation of the matrix during the 3D printing. However, the value of the polydispersity index remained fairly constant (PDI = 1.4 and 1.3 for pellets and 3D parts, respectively). This degradation was mainly due to the hydrolytic degradation of PDLLA (Codari et al. 2012).

Model prediction of healing in DPPE

As it is known with other additive manufacturing techniques, for DPPE, the interlayer bonding takes place between the adjacent layers through a combination of polymer deformation, cooling, surface wetting, chains diffusion at the interface, and finally chains entanglement (Seppala et al. 2017).

Modeling of the effect of the entanglement rate on the equivalent relaxation time

As studied in our previous works, (Zhang et al. 2015, 2016), the extrusion process induces chain orientation and may influence the rate of chain interdiffusion. During DPPE, the polymer experiences temperatures and large shear rates in the nozzle that affect its microstructure. Previous studies, (McIlroy and Olmsted 2017b, a; Costanzo et al. 2020; Gilmer et al. 2021), have modeled the flow-induced disentanglement and welding under 3D material extrusion conditions. Herein, we propose using the non-linear Convective Constrain release model presented by Ianniruberto et al. (2014) to develop a modeling approach to account the re-entanglement in DPPE.

Table 1 Material properties, main viscoelastic parameters of PDLLA at 190 °C and molecular weight of granulates and printed parts

Polymer	$\rho (gcm^{-3})$ 190°C[1]	Gc (MPa)	$\eta_0 (Pas)$	τ_n (ms)	$G_N^0 (MPa)$	Ze (Mw/Me)	$\tau_w (ms)$	*(pellets)* $M_w (kg/mol)$[2]	*(3D parts)* $M_w (kg/mol)$[2]	$R_g (nm)$[3]
PDLLA	*1.11*	*0.10*	*2260*	*5.1*	*0.45*	*14*	*23*	*133.8*	*92.3*	*17.6*

[1] Determined from (Fang and Hanna 1999). [2] Calculated by steric extrusion chromatography (SEC) in chloroform. [3] From 3D parts calculated using the light scattering detector

Our goal is to calculate the interphase thickness (χ) as a function of time, temperature, shear rate, and shear deformation during extrusion and deposition. Indeed, to fulfill that goal it is necessary to consider the effect of chain orientation and deformation by introducing a disentanglement factor,υ, into the calculation of the equivalent relaxation time, $\tau_{w,eq}$, from CCR model following the relationship:

$$\tau_{w,eq} = \tau_w \upsilon^{1.2} \tag{9}$$

The 1.2 power is given according to the well-known 3.4 power law for the terminal-relaxation-time dependence on the molecular mass of entangled polymers (Ianniruberto and Marrucci 2014).

As aforementioned, the PDLLA was extruded through a nozzle with a high shear rate (depending on the printing speed). During the material extrusion/print deposition, an alignment of the chains is obtained when the experimental time becomes shorter than the reptation time ($1/\dot{\gamma} < \tau_w$), in other words, the Weissenberg number satisfies $Wi_w > 1$ ($Wi_w = \dot{\gamma}\tau_w$). At high shear rates, when the Rouse Weissenberg number $Wi_R > 1$ ($Wi_R = \dot{\gamma}\tau_R$), the chains are considered to be highly stretched (Graham et al. 2003). Considering our experimental conditions, $U_N = 30\text{mm/s}$, $T_{nozzle} = 190°C$, $H = 0.2\text{mm}$ and a $D_{nozzle} = 0.4\text{mm}$, we assume that the chains present an orientation through the flow direction without stretching of the tube confining the chain ($Wi_w = 11.49$ and $Wi_R = 0.15$).

When the filament exits the nozzle at a temperature T, the melt experiences a deformation during the deposition time (τ_{dep}) imposed by the printing parameters such as the nozzle diameter, layer thickness, layer width, and printing speed. In this case, $\tau_{dep} = H/U_N = 0.0067\text{s}$ ($\tau_R < \tau_{dep} < \tau_{w,eq}$). As described before, after deposition, the temperature drops rapidly to a value close to T_g and at the same time, entanglements are recreated at the interphase between the layers as described by Eq. 10. As the polymer chains present an orientation in the flow direction, they become partially disentangled quickly after the extrusion. In addition, due to the cooling, these entanglements may not be able to fully re-create an interphase since oriented chains may not have sufficient time to diffuse across the interface. Thus, the interphase presents a delay in entanglement recovery. For each following printed layer, the previous interfaces experience an increase in temperature and so the degree of healing progressively increases in a delayed fashion.

The rate of entanglement, $d\upsilon$/dt (Eq. 10)**,** is described as the difference between the rate of loss and re-creation of entanglements

$$\frac{d\upsilon}{dt} = -r_{loss} + r_{recr} = -\beta_{CCR}\left(k : S - \frac{1}{L}\frac{dL}{dt}\right)\upsilon + \frac{1-\upsilon}{\tau_w} \tag{10}$$

here, β_{CCR} is the convective constraint release parameter, k is the velocity gradient tensor, S the orientation tensor, and L the average tube length at time t. After deposition, healing starts with $k = 0$:

$$\frac{d\upsilon}{dt} = \beta_{CCR}\upsilon\frac{1}{L}\frac{dL}{dt} + \frac{1-\upsilon}{\tau_w} \tag{11}$$

with the following initial condition (Eq. 12) determined by the extrusion flow and filament deposition parameters (McIlroy and Olmsted 2017b):

$$\upsilon(0) = \frac{1}{1 + \beta_{CCR}\gamma Wi_w} \tag{12}$$

where γ is the shear deformation during deposition ($\gamma = \dot{\gamma}\tau_{dep}$). Moreover, as during filament extrusion and deposition the chains present an orientation through the flow direction without stretching of the tube (L becomes independent of time and $dL/dt = 0$), the final entanglement can be predicted from Eq. 11 as follows:

$$\upsilon(t) = 1 - (1 - \upsilon(0))\exp\left(\frac{-t}{\tau_w(T)}\right) \tag{13}$$

here, the healing temperature is considered as constant. However, as welding is produced under non-isothermal conditions, the entanglement fraction calculated in the previous equation can be changed to (Eq. 14):

$$\upsilon(t) = 1 - (1 - \upsilon(t - \Delta t))\exp\left(\frac{-\Delta t}{\tau_w(T(t))}\right) \tag{14}$$

with Δt the time step over which the temperature is considered constant and it is used to adjust the sensitivity of the model.

Eventually, Eq. 14 considers the flow-induced orientation during the transient step of polymer extrusion and deposition as well as the effect of temperature during the interfacial diffusion between layers. Figure 6 shows our modeling evolution of the entanglement rate, at different printing speeds and temperatures, and its impact on the post-deposition cooling. The initial entanglement rate, $\upsilon(0)$, is influenced by the shear rate and therefore by the printing speed. Even if the value of $\upsilon(0)$ decreased as a function of printing speed, as shown in Fig. 6a, a completely re-entanglement is ensured at the end of filament deposition for a printing temperature of 190 °C. The chains reach a complete recovery of the entanglements for high printing temperatures (190–160 °C). However, for lower temperatures (below 160 °C), the entanglement rate at long times remains lower than 1 since when the filament reaches the plateau temperature the polymer chain mobility is already too highly reduced to enable full re-entanglement. Moreover, considering a constant printing speed, $\upsilon(0)$ values decrease for lower printing temperatures. Thus, for a printing temperature of 190 °C, a complete recovery of the

Fig. 6 Example of entanglement rate evolution after filament deposition for **a** different printing speed at 190 °C and **b** different extrusion temperatures with $U_{\mathrm{N}} = 30\mathrm{mm/s}$

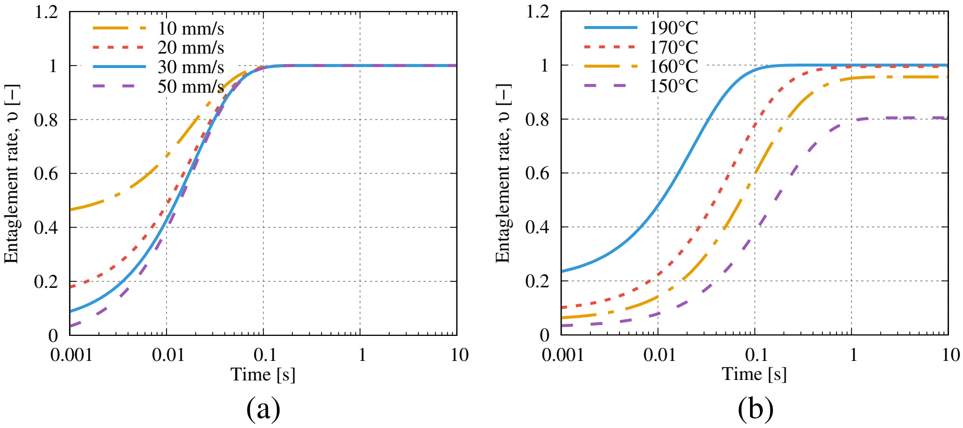

(a) (b)

entanglements is estimated at 0.1 s after deposition. In conclusion, this modeling approach allows us to calculate the effect of flow-induced chain alignment on the healing process (i.e., chain interdiffusion at the interphase) of a PDLLA during DPPE for a different given temperatures and printing speeds.

Figure 7 shows the relaxation dynamics during filament cooling for different printing temperatures. The parameters used for $\tau_{\mathrm{w,eq}}$ calculation are $\beta_{\mathrm{CCR}} = 0.3$ and $\dot{\gamma} = 600\mathrm{s}^{-1}$ (printing shear rate at the nozzle). As mentioned before (Eq. 9), this equivalent reptation time depends on the number of entanglements. At short times, fewer entanglements are recovered due to the lower initial value of entanglements υ, thereby, as shown in the purple curve, the chains reptate faster than in equilibrium. At high temperatures, the polymer is able to diffuse faster and the entanglements become fully recovered at short times ($Z_{\mathrm{e,eq}} = Z_{\mathrm{e}}$, with Z_{e} the number of entanglements at equilibrium). However, for lower temperatures, $Z_{\mathrm{e,eq}} > Z_{\mathrm{e}}$, there are less entanglements which facilitated the reptation of the chain but the final part still presents still a partially re-entangled polymer (Supporting Information A).

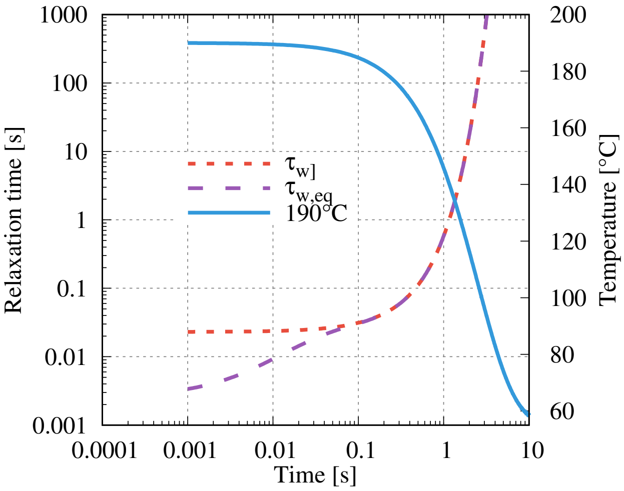

Fig. 7 Relaxation dynamics after filament deposition for a printing temperature of 190 °C

Modelling the interdiffusion thickness (χ)

In the transient regime observed after filament deposition, the interdiffusion thickness (χ) depends on time as $\chi \propto t^{\alpha}$ (Bousmina et al. 1998). The dynamics of entangled polymer chains inside the confining tube can be described by different relaxation times as (De Gennes 1979; Doi and Edwards 1986):

$$\phi_{\mathrm{n}}(\mathrm{t}) \sim \begin{cases} \mathrm{t}^{1/4} \text{ for } \mathrm{t} < \tau_e \\ \mathrm{t}^{1/8} \text{ for } \tau_{\mathrm{e}} < \mathrm{t} < \tau_{\mathrm{R}} \\ \mathrm{t}^{1/4} \text{ for } \tau_{\mathrm{R}} < \mathrm{t} < \tau_{\mathrm{rep}} \\ \mathrm{t}^{1/2} \text{ for } \mathrm{t} > \tau_{\mathrm{rep}} \end{cases} \tag{15}$$

However, the self-diffusion of a chain in the bulk is different from the chain motion across an interface. The diffusion mechanism at the interface depends on the configuration of the chain ends at the initial time of diffusion.

$\chi(t)$ is defined by the diffusion coefficient, $\mathrm{D_s}$, and the healing time, t_{h}. For symmetrical diffusion and under isothermal conditions, the interfacial thickness can be described by the following relation (Lamnawar et al. 2012; Zhang et al. 2013):

$$\chi(t) = 2(\mathrm{D_s t_h})^{1/2} \tag{16}$$

With the self-diffusion coefficients, $\mathrm{D_s}$, of macromolecular chains that can be modeled either with Rouse dynamics ($\mathrm{D_R}$) or with reptation dynamics developed by the Doi–Edwards theory ($\mathrm{D_{rep}}$)Lamnawar et al. 2012; Zhang et al. 2013):

$$\mathrm{D_R} = \frac{\mathrm{k_b T}}{\xi \mathrm{N}} \tag{17}$$

$$\mathrm{D_{rep}} = \frac{\mathrm{k_b T e^2}}{3\xi \mathrm{N^2 b^2}} \tag{18}$$

With $k_{\mathrm{b}} = 1.38 \cdot 10^{-23} N \cdot m \cdot K^{-1}$ is the Boltzmann constant, $b = 0.72nm$ is the polymer Kuhn-length, N the number of segments of the polymer chain and the step length, e, determined as:

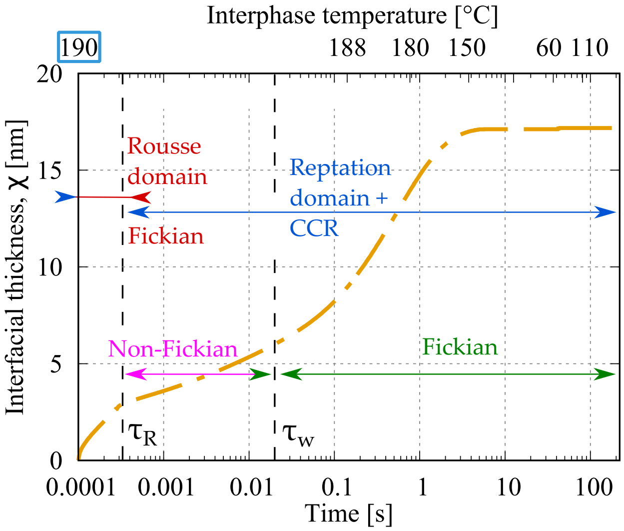

Fig. 8 Interfacial thickness evolution between layers 1 and 2 during 3D printing with the corresponding temperature for a nozzle temperature of 190 °C. The arrows indicate the different domains used to calculate the interfacial thickness

$$e = b\left(\frac{4}{5}\frac{M_e}{M_0}\right)^{0.5} \tag{19}$$

The monomeric friction coefficient (ξ) is determined from Time–temperature superposition master curves at the crossover of the G' and G'' curves and with the corresponding relaxation time (τ_n) (Ferry 1980).

$$\xi(T) = \frac{3\tau_n}{k_b T}\left(\frac{4M_0G_c}{b\rho N_0}\right)^2 \tag{20}$$

Here, $M_0 = 72g \cdot mol^{-1}$ is the molecular mass of one segment, N_0 is the Avogadro constant, ρ the polymer density at a given temperature, and G_c the modulus at the intersection of G' and G''.

Previous studies have defined the diffusion across the interface by a combination of a Fickian and non-Fickian regimes (Wool et al. 1989; Bousmina et al. 1998; Lamnawar et al. 2012; Zhang et al. 2012). For $t_h < \tau_R$ and $t_h > \tau_{rep}$ the kinetics diffusion is governed by Fick's law, whereas for $\tau_R < t_h < \tau_{rep}$, the chain dynamics is composed by both Rouse and reptation motion (Fig. 8). For the diffusion that occurred at $t < \tau_R$, D_s is determined by the Rouse model (Eq. 17) and for $t_h > \tau_{rep}$ by the reptation dynamics (Eq. 18). However, for $\tau_R < t_h < \tau_w$, the diffusion coefficient is influenced by a contribution of both motions. To simplify the contributions of the Rouse and reptation relaxations, the calculation of the interphase thickness and the healing time was divided in two parts where $t_h < \tau_R$ followed the Rouse model and $t_h > \tau_R$ the reptation model.

However, as observed in previous sections, the temperature in DPPE varies during the deposition time and affects the chain mobility. Thus, the interphase thickness needs to be described as:

$$\chi(t_h) = 2\left(\int_0^t D_s(T, \dot{\gamma})dt_h\right)^{1/2} \tag{21}$$

Figure 8 shows the evolution of the interphase thickness between layers 1 and 2 during the 3D printing process considering the disentanglement effect after extrusion. The two regimes are distinguished. The different interphases between successive layers exhibit similar behavior since the chain interpenetration occurs during the very first seconds after deposition. The reheating produced by the deposition of subsequent layers does not induce a significant increase on the length of previous interphases.

Modeling the healing degree (D_h)

The level of adhesion between printed layers is defined as the ratio of the interfacial bond strength with respect to the ultimate bond strength of the bulk material, hereafter defined as the degree of healing (D_h)(Yang and Pitchumani 2002). The ultimate bond strength is achieved when the chains are completely relaxed ($t_h \geq \tau_w$) or equivalently, when the interdiffusion thickness (χ) reaches an equivalent length to the radius of gyration (R_g). Equation 22

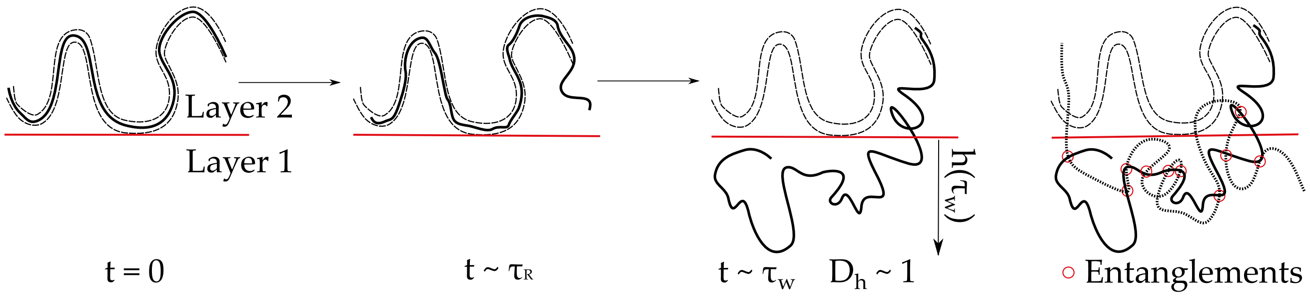

Fig. 9 Relaxation dynamics of the interphase after filament deposition

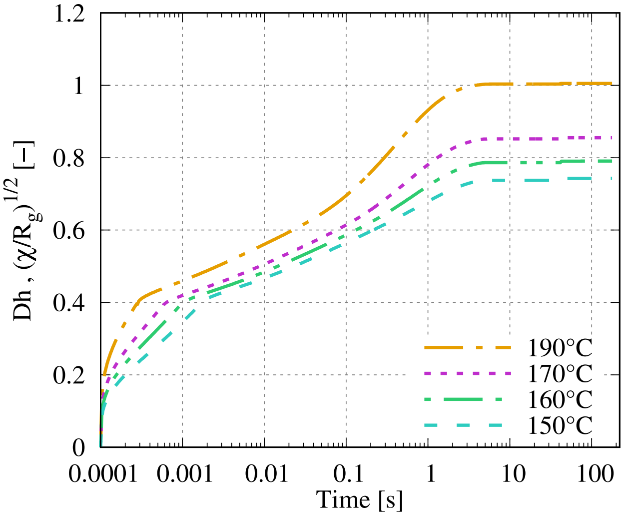

Fig. 10 Evolution of healing degree D_h after deposition calculated from the interphase thickness for PDLLA at different printing temperatures for the interphase between layers 1 and 2

Table 2 Interfacial thickness and degree of healing of different layers

	Layer 0/1	*Layer 1/2*	*Layer 2/3*	*Layer 3/4*
$\chi(nm)$	19.2	17.2	17.2	23
D_h	1.04	0.99	0.99	1.14

expresses the relationship between the degree of healing, D_h, the welding time (t_h) and the equivalent relaxation time (hereafter referred as τ_w), the interphase thickness (χ) and the radius of gyration (R_g) (Das et al. 2021):

$$\mathrm{D_h(T,t)} = \left(\frac{\mathrm{t_h}}{\tau_\mathrm{w}}\right)^{\frac{1}{4}} = \left(\frac{\chi(\mathrm{t_h})}{\mathrm{R_g}}\right)^{\frac{1}{2}} \tag{22}$$

The calculation for D_h based on the relaxation time (τ_w) is explained in supporting information A.

Figure 9 shows the chain relaxation dynamics after filament deposition and the newly formed entanglements at the interphase for $t_\mathrm{h} \sim \tau_\mathrm{w}$.

The theoretical evolution of D_h calculated from the value of χ as a function of deposition time for different printing temperatures are shown in Fig. 10. Only the printing temperature at 190 °C exhibited a $D_\mathrm{h} \geq 1$. Besides, in the case of different layers printed at 190 °C, the predicted interphase thickness exhibits a value higher than R_g (Table 2), and thus, by definition, a fully healed interphase. Hereby, the measurements of temperature as a function of deposition time confirmed the 100% welding between the different layers.

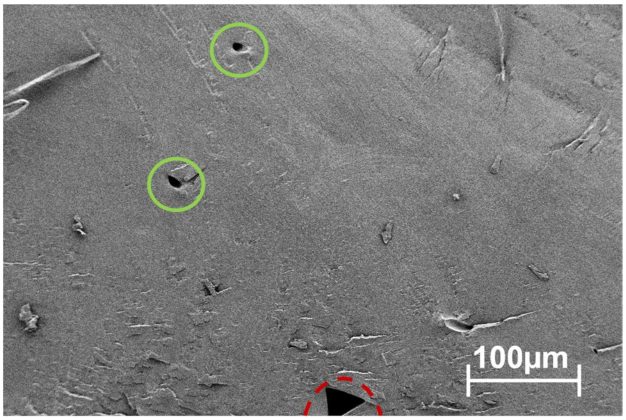

Fig. 11 Scanning electron micrographs of cross sections taken in bulk specimens of neat PDLLA

Experimental characterization and model validation

Microstructural characterization

The manufacturing process has an important effect on the presence of voids which will have strong consequences on the final mechanical properties of the printed material. Even with a printing parameter corresponding to 100% filling, a small fluctuation of flow during extrusion can provoke a non-perfect contact between adjacent filaments, and consequently the apparition of internal pores in some samples (with a size ranging between 20 and 200 µm). In this study, we observe the presence of internal porosity in all specimens.

The SEM analysis of the cryogenically fractured surface, illustrated in Fig. 11, confirms a correct printing quality with a good welding between the different filament layers. Two families of voids can also be distinguished in Fig. 11: larger voids between different deposited filaments (triangles with a length of ~ 15–60 µm) and smaller voids inside the filaments. The former is the consequence of the typically flattened ellipsoidal filament shape when deposited. Meanwhile, small voids are the intra-filament pores specific to parts fabricated by a 3D printing extrusion process (Tao et al. 2021).

Mechanical characterization

The mechanical properties of printed DDPE parts were examined. As often observed in additive manufacturing, the tensile results for printed specimens displayed a higher degree of brittle failure than injected samples. Table 3

Table 3 Mechanical properties of PDLLA parts fabricated by 3D printing and injection molding

	$\sigma_{max}(MPa)$	$E(MPa)$	$\varepsilon_{break}(\%)$
Injection molding	59 ± 1.4	1460 ± 30	5.7 ± 0.4
3D printing	48 ± 3	1470 ± 140	4 ± 0.5

Table 4 Degree of healing with the corresponding time and temperature healing for the lap-shear test

T (°C)	T (min)	Dh (−)
70	3	0.3
80	3	0.4
80	8	0.5
90	2	0.8

compares the maximum tensile strength (σ_{max}) the Young's modulus (E) and the deformation at break (ε_{break}) for samples fabricated by DPPE and injection molding. A lower average value and larger error bars for DPPE samples than injected samples indicated weaker mechanical properties due to the presence of defects such as the previously observed internal porosities.

Validation of the proposed model by the crack healing theory

Different healing times and temperatures have been applied to model bilayers prepared by compression molding under controlled processing parameters in order to characterize the mechanical properties for different qualities of welding of PDLLA, and thus different theoretical healing degrees. Table 4 shows the corresponding degrees of healing for each coupled time–temperature healing.

In the lap shear tests, we observed 3 types of fractures: cohesive, adhesive, and stock-break (Fig. 12a). These three types of fracture confirm that a robust interface is a signature of good interdiffusion during the healing process. However, for the sake of good interpretation of lap shear tests, only the results of cohesive fracture tests were used to determine the shear strength of the interphase (Awaja et al. 2009). For adhesive failure, we can only say that the healed interphase presented a better adhesion that the sample to (steel) substrate bonding. In the case of specimens with $D_h > 0.8$, we observed a stock-break failure. The fracture took place in a stress concentration location for the bulk material. Therefore, in this third case, the interphase presented a superior strength than that of this stress-concentrated corner of the bulk material. The results of normalized lap-shear strength measurements for PDLLA at different temperatures and degrees of healing are shown in Fig. 12b ($\sigma_{weld}/\sigma_{bulk}$ increased linearly with $t_h^{1/4}$) .

In order to compare the level of healing obtained by 3D printing, several lap-shear tests were performed with samples manufactured by DPPE. However, all the printed samples showed a stock-break failure; thus, limiting the quantitative interpretation of the results. Nonetheless, it seems that the adhesively printed parts presented good enough adhesion between the different layers that the material preferentially broke in the stress concentration

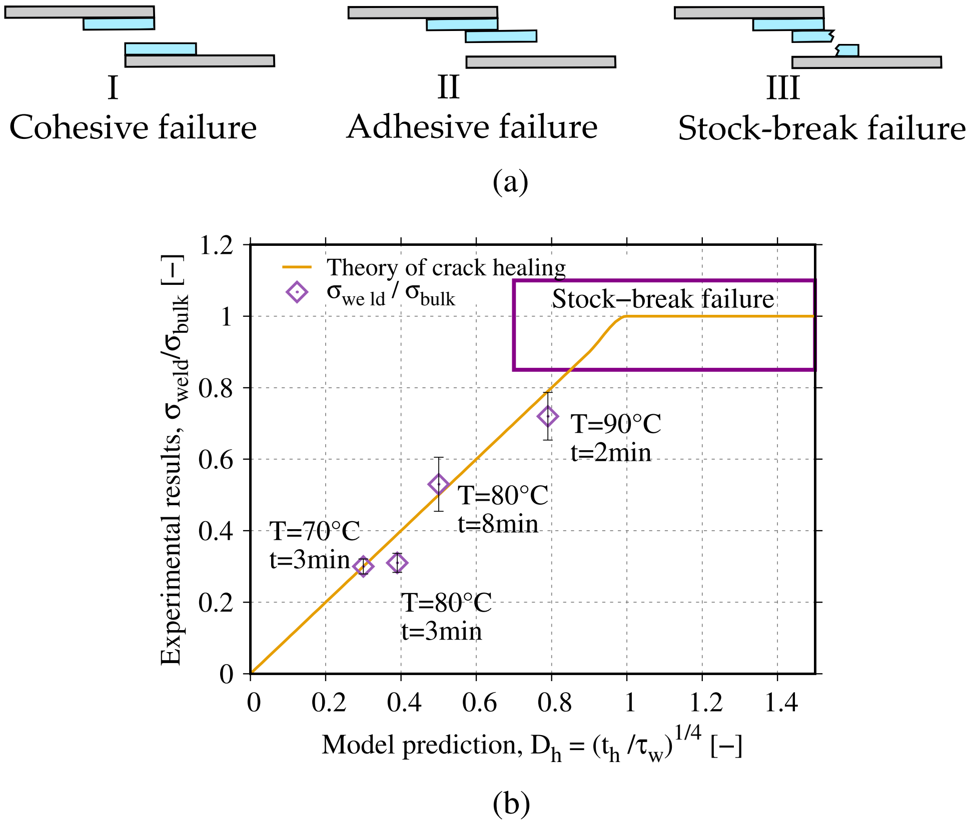

Fig. 12 **a** Representation of lap-shear system and the different failures modes observed in the tests and **b** experimental results from lap-shear test ($\sigma_{weld}/\sigma_{bulk}$) vs model prediction $\left(t_h/\tau_w\right)^{\frac{1}{4}}$ for PDLLA, purple square represents the zone with a stock-break failure

region of the stock-break failure mode. Based on the results obtained from lap-shear tests on compression molded samples, we can hypothesize that the 3D-printed parts presented at least a $D_h > 0.8$.

Conclusions

The objective of this work was to present a combined experimental and modeling approach focusing on the rheology of filament deposition in order to gain a deeper understanding of the welding process occurring between them, and consequently of the final morphological and mechanical properties of printed PDLLA systems by the innovative DPPE process.

The temperature profile in between layers during the 3D printing of a dumbbell-shaped specimen was firstly measured and subsequently modeled. In parallel, the rheological properties of PDLLA in SAOS, and capillary rheometry were characterized in order to estimate the viscosity as a function of the temperature and shear-rate in the nozzle during 3D printing. Both studies allowed us to obtain the required input parameters for the healing process modelling.

Throughout this work, we presented a systematic approach studying how the process parameters, thermal profiles, and predicted polymer diffusion at the interphase influenced the degree of healing and eventually the final strength of PDLLA printed parts via the DPPE process. Our approach was based on the CCR model, the crack healing theory, and the reptation model incorporating a non-isothermal diffusion analysis. In our approach, we introduced the calculation of the interphase thickness from self-diffusion coefficient and took into account the entanglement rate. We thus highlighted that it is possible to introduce non-isothermal polymer relaxation and chain orientations into the modeling of entanglement rate by using the Convective constraint release model (CCR) theory. Moreover, heat transfer predictions demonstrated that small changes of printing temperature can result in significant differences in the predicted value of D_h. The modeling of D_h from the interphase thickness (χ), indicated that the healing process mainly occurs at high temperature, thus, during the first seconds after deposition. The cross-section observed by the microstructural analysis confirmed a good welding between adjacent filaments. In addition, the experimental validation by lap-shear tests provided a complementary approach to the understanding of the healing in the 3D printing process. The performed tensile properties and lap shear results confirmed the creation of a robust interphase and corroborated our modeling findings.

Additionally, DPPE demonstrated a 3D printing potential to create well-designed structures with relatively good mechanical properties and complex geometries. Further investigations regarding the capability of using multi-screw-based extrusion to construct 3D geometries with different compositions and controllable structures are envisioned in the future to further show the large possibilities of this additive manufacturing process.

In summary, the present findings reveal how rheology and physically-based modeling are suitable tools to probe interfacial properties build up, and, moreover, through this approach, we rationalize the importance of their control during DPPE manufacturing to optimize the final mechanical properties.

Supplementary Information The online version contains supplementary material available at https://doi.org/10.1007/s00397-022-01377-6.

Acknowledgements X.L would like to thank "MESRI" for financial support for his PhD studies. The authors gratefully acknowledge Dr. Guilhem Baeza (MATEIS) for the fruitful discussions regarding the CCR model and Jérôme Adrien (MATEIS) for the "tomography" analyses. We thank the Liquid Chromatography Characterization Polymer Center of Institut de Chimie de Lyon (Agnes Crepet, IMP) for assistance and access to the SEC facilities.

References

Awaja F, Gilbert M, Kelly G et al (2009) Adhesion of polymers. Prog Polym Sci 34:948–968. https://doi.org/10.1016/j.progpolymsci.2009.04.007

Boudara VAH, Read DJ, Ramírez J (2020) Reptate rheology software : Toolkit for the analysis of theories and experiments. J Rheol (N Y N Y) 709. https://doi.org/10.1122/8.0000002

Bousmina M, Qiu H, Grmela M, Klemberg-Sapieha JE (1998) Diffusion at polymer/polymer interfaces probed by rheological tools. Macromolecules 31:8273–8280. https://doi.org/10.1021/ma980562r

Cicala G, Giordano D, Tosto C et al (2018) Polylactide (PLA) filaments a biobased solution for additive manufacturing : correlating rheology and thermomechanical properties with printing quality. Materials (basel). https://doi.org/10.3390/ma11071191

Codari F, Lazzari S, Soos M et al (2012) Kinetics of the hydrolytic degradation of poly (lactic acid). Polym Degrad Stab 97:2460–2466. https://doi.org/10.1016/j.polymdegradstab.2012.06.026

Corcione CE, Gervaso F, Scalera F et al (2017) 3D printing of hydroxyapatite polymer-based composites for bone tissue engineering. J Polym Eng 37:741–746. https://doi.org/10.1515/polyeng-2016-0194

Costa SF, Duarte FM, Covas JA (2015) Thermal conditions affecting heat transfer in FDM/FFE: a contribution towards the numerical modelling of the process. Virtual Phys Prototyp 10:35–46. https://doi.org/10.1080/17452759.2014.984042

Costa SF, Duarte FM, Covas JA (2017) Estimation of filament temperature and adhesion development in fused deposition techniques. J Mater Process Technol 245:167–179. https://doi.org/10.1016/j.jmatprotec.2017.02.026

Costanzo A, Spotorno R, Candal MV, et al (2020) Residual alignment and its effect on weld strength in material-extrusion 3D-printing of polylactic acid. Addit Manuf 36. https://doi.org/10.1016/j.addma.2020.101415

Das A, Gilmer EL, Biria S, Bortner MJ (2021) Importance of polymer rheology on material extrusion additive manufacturing: correlating process physics to print properties. ACS Appl Polym Mater 3:1218–1249. https://doi.org/10.1021/acsapm.0c01228

De Gennes P-G (1979) Scaling concepts in polymer physics. Cornell University Press, Ithaca

Do Vale Pereira R, Salmoria GV, De Moura MOC et al (2014) Scaffolds of PDLLA/bioglass 58S produced via selective laser sintering. Mater Res 17:33–38. https://doi.org/10.1590/S1516-14392014005000075

Doi M, Edwards SF (1986) The theory of polymer dynamics. Oxford University Press, New York

Fang Q, Hanna MA (1999) Rheological properties of amorphous and semicrystalline polylactic acid polymers. Ind Crops Prod 10:47–53. https://doi.org/10.1016/S0926-6690(99)00009-6

Ferry JD (1980) Viscoelastic properties of polymers, Third Edit. Wiley, Chichester

Gilmer EL, Anderegg D, Gardner JM, et al (2021) Temperature, diffusion, and stress modeling in filament extrusion additive manufacturing of polyetherimide: an examination of the influence of processing parameters and importance of modeling assumptions. Addit Manuf 48. https://doi.org/10.1016/j.addma.2021.102412

Gradwohl M, Chai F, Payen J et al (2021) Effects of two melt extrusion based additive manufacturing technologies and common sterilization methods on the properties of a medical grade PLGA copolymer. Polymers (basel) 13:572. https://doi.org/10.3390/polym13040572

Graham RS, Likhtman AE, McLeish TCB, Milner ST (2003) Microscopic theory of linear, entangled polymer chains under rapid deformation including chain stretch and convective constraint release. J Rheol (n Y N y) 47:1171–1200. https://doi.org/10.1122/1.1595099

Ianniruberto G, Marrucci G (2014) Convective constraint release (CCR) revisited. J Rheol (n Y N y) 58:89–102. https://doi.org/10.1122/1.4843957

Lamnawar K, Bousmina M, Maazouz A (2012) 2D encapsulation in multiphase polymers: Role of viscoelastic, geometrical and interfacial properties. Macromolecules 45:441–454. https://doi.org/10.1021/ma201151k

Lepoivre A, Boyard N, Levy A, Sobotka V (2020) Heat Transfer and Adhesion Study for the FFF Additive Manufacturing Process. Procedia Manuf 47:948–955. https://doi.org/10.1016/j.promfg.2020.04.291

McIlroy C, Olmsted PD (2017a) Disentanglement effects on welding behaviour of polymer melts during the fused-filament-fabrication method for additive manufacturing. Polymer (guildf) 123:376–391. https://doi.org/10.1016/j.polymer.2017.06.051

McIlroy C, Olmsted PD (2017b) Deformation of an amorphous polymer during the fused-filament-fabrication method for additive manufacturing. J Rheol (n Y N y) 61:379–397. https://doi.org/10.1122/1.4976839

Pei X, Ma L, Zhang B, et al (2017) Creating hierarchical porosity hydroxyapatite scaffolds with osteoinduction by three-dimensional printing and microwave sintering. Biofabrication 9.https://doi.org/10.1088/1758-5090/aa90ed

Peñas MI, Calafel MI, Aguirresarobe RH et al (2020) How is rheology involved in 3D printing of phase-separated PVC-acrylate copolymers obtained by free radical polymerization. Polymers (Basel) 12. https://doi.org/10.3390/POLYM12092070

Seppala JE, Hoon Han S, Hillgartner KE et al (2017) Weld formation during material extrusion additive manufacturing. Soft Matter 13:6761–6769. https://doi.org/10.1039/C7SM00950J

Tao Y, Kong F, Li Z et al (2021) A review on voids of 3D printed parts by fused filament fabrication. J Mater Res Technol 15:4860–4879. https://doi.org/10.1016/j.jmrt.2021.10.108

Vanaei HR, Shirinbayan M, Costa SF et al (2021) Experimental study of PLA thermal behavior during fused filament fabrication. J Appl Polym Sci 138:49747. https://doi.org/10.1002/app.49747

Wool RP, O'Connor KM (1981) A theory crack healing in polymers. J Appl Phys 52:5953–5963. https://doi.org/10.1063/1.328526

Wool RP, Yuan B-L, McGarel OJ (1989) Welding of polymer interfaces. Polym Eng Sci 29:1340–1367. https://doi.org/10.1002/pen.760291906

Yang F, Pitchumani R (2002) Healing of thermoplastic polymers at an interface under nonisothermal conditions. Macromolecules 35:3213–3224. https://doi.org/10.1021/ma010858o

Zhang H, Lamnawar K, Maazouz A (2012) Rheological modeling of the diffusion process and the interphase of symmetrical bilayers based on PVDF and PMMA with varying molecular weights. Rheol Acta 51:691–711. https://doi.org/10.1007/s00397-012-0629-7

Zhang H, Lamnawar K, Maazouz A (2013) Rheological modeling of the mutual diffusion and the interphase development for an asymmetrical bilayer based on PMMA and PVDF model compatible polymers. Macromolecules 46:276–299. https://doi.org/10.1021/ma301620a

Zhang H, Lamnawar K, Maazouz A (2015) Fundamental understanding and modeling of diffuse interphase properties and its role in interfacial flow stability of multilayer polymers. Polym Eng Sci 55:771–791. https://doi.org/10.1002/pen.23945

Zhang H, Lamnawar K, Maazouz A, Maia JM (2016) A nonlinear shear and elongation rheological study of interfacial failure in compatible bilayer systems. J Rheol (n Y N y) 60:1–23. https://doi.org/10.1122/1.4926492

Zhou Z, Salaoru I, Morris P, Gibbons GJ (2018) Additive manufacturing of heat-sensitive polymer melt using a pellet-fed material extrusion. Addit Manuf 24:552–559. https://doi.org/10.1016/j.addma.2018.10.040